Inorganic Chemistry

pubs.acs.org/IC

Article

# Correlation between Cation Distribution and Magnetic and Dielectric Properties of $Dy^{3+}$-Substituted Fe-Rich Cobalt Ferrite

Shahaji P. Kharat, Swati K. Gaikwad, Rahul C. Kambale, Yesh D. Kolekar,* and C. V. Ramana*

Cite This: *Inorg. Chem.* 2022, 61, 19319−19332

Read Online

**ABSTRACT:** Designing electromagnetic materials, particularly those based on transition-metal-containing spinel ferrites, with a controlled structure, phase, and chemistry at the nanoscale dimensions while realizing enhanced electrical and magnetic properties continues to be a challenging problem. Herein, we report on the synthesis and structure−property correlation of dysprosium (Dy)-substituted iron-rich cobalt ferrite ($Co_{0.8}Fe_{2.2-x}Dy_xO_4$; CFDO; $x$ = 0.000−0.100) oxides with variable $Dy^{3+}$ concentration. Chemical bonding analyses of CFDO nanomaterials using Raman spectroscopic analyses supported the spinel phase formation with high quality. Cation distribution determined from Mössbauer spectroscopy reveals the fact that $Dy^{3+}$ occupies the octahedral site of the spinel lattice. Saturation magnetization ($M_s$) values calculated using Neel's two-sublattice model and cation distribution derived from Mossbauer's studies correlate well with the magnetization values obtained from SQUID measurements. The B-site hyperfine field decreases from 52.24 ± 0.10 to 49.26 ± 0.00 T, as evidenced by the Mössbauer spectra, with Dy substitution, which decreases the Fe-ion occupancy from the octahedral site of CFDO. Frequency-dependent dielectric constant indicates electron hopping in the grain interior, which ceases above 6.3 kHz. Dielectric measurements indicate that these CFDO compounds are useful for absorption at higher frequencies. Thus, using the combined approach based on Raman and Mössbauer spectroscopic analyses, the present work elucidates the structure, chemical bonding, and magnetic properties of Dy-substituted Fe-rich cobalt ferrite. CFDO may serve as a model system to apply to a class of Fe-rich ferromagnetic nanomaterials for electromagnetic and sensor applications.

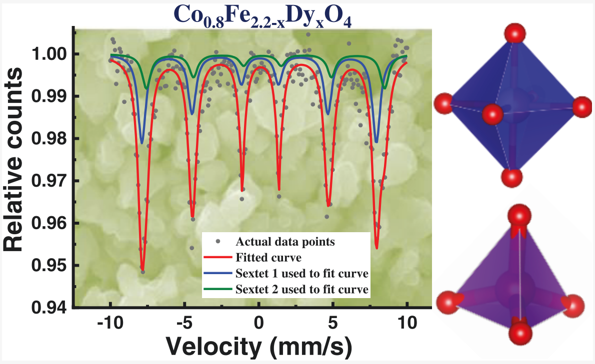

## INTRODUCTION

Spinel ferrites continue to attract the attention of the scientific and research community for the design and development of smart materials for application in numerous technologies.[1−16] All spinel ferrites, which can be represented by the universal chemical formula $MFe_2O_4$ (where Fe exists in the trivalent state ($Fe^{3+}$), and "M" represents divalent cations such as $Zn^{2+}$, $Ni^{2+}$, $Co^{2+}$, etc.), crystallize (see Figure 1) in the $Fd\bar{3}m$ space group.[2,7] By virtue of tunable magnetic properties and the ability to obtain materials with variable morphology and magnetic behavior, cobalt ferrites (CFO) have been subjected to extensive studies in recent years. Additionally, CFO exhibit excellent thermal and chemical stability.[17] All of these properties make cobalt ferrite an excellent candidate for many industrial applications.[17−20] At present, CFO are at the center of research activities, where efforts are primarily directed to obtain enhanced and/or variable properties by simply doping different cations with varying amounts.[14,17−24] The attention given to intrinsic or doped-CFO is primarily due to their fundamental properties and potential applications in different areas, such as magnetic hard drives,[1,4,6] magnetic ferrofluid technology,[4,10] magnetocaloric refrigeration,[10] chem-

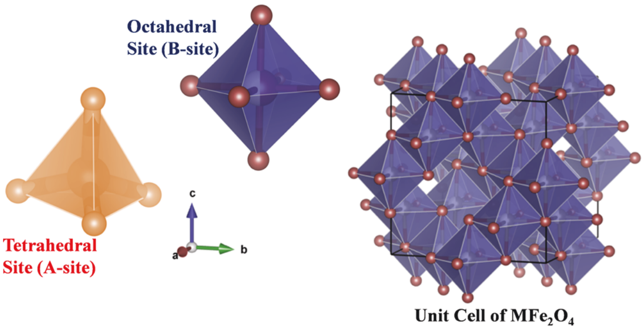

**Figure 1.** Crystal structure of a cubic spinel ferrite with a chemical formula of $MFe_2O_4$. The unit cell, tetrahedral (A) site, and octahedral (B) site are represented.

**Received:** September 1, 2022
**Published:** November 23, 2022

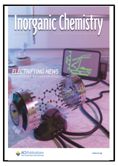

https://doi.org/10.1021/acs.inorgchem.2c03125
*Inorg. Chem.* 2022, 61, 19319−19332

ical sensors,[4,6,7] photocatalysis and cleaner fuel production,[15] rod antennas, good-quality filters and magnetic field sensors,[4,6,7,12,25] and magnetostrictive phase in magnetoelectric (ME) composite materials.[13] Furthermore, cobalt ferrite, owing to its magnetocrystalline anisotropy, high coercivity, and chemical stability, has been used widely in automotive and environmental engineering.[14,17] In these fields, special attention is given to device applications, such as sensors, environmental protection, catalysis, microwave absorption, etc.[17] However, the properties and performance characteristics of these ferrites are dependent on the structure, chemistry, and cation distribution, which in turn depend on the methods of preparation, processing conditions, and dopant ions (if any).[7−9,16,26] Most importantly, the structural, magnetic, electrical, and dielectric properties of spinel ferrite materials greatly depend on the chemistry and precise distribution of cations.[7,16,26] Furthermore, in the spinel ferrite system, which exhibits two crystallographically distinguishable sublattices such as tetrahedral site (A-site) and octahedral site (B-site) (Figure 1) in the general $MFe_2O_4$ spinel structure, the distribution of cations is also highly important, especially when using other dopant ions to derive tunable properties.[7,16] Structurally, depending on the distribution of cations at tetrahedral or octahedral sites (Figure 1), the resulting material may be in a normal, inverse, or mixed spinel structure.

Rare-earth substitution ($Gd^{3+}$, $Dy^{3+}$, $Er^{3+}$, etc.) in cobalt ferrite is extensively studied due to the highly interesting and tunable magnetic properties of the resulting materials.[3,27−29] However, for intrinsic and substituted/doped nanoferrites, the properties and performance characteristics are significantly affected by the particle size, size distribution, and cation distribution at A- and B-sites in the crystal structure.[16,19−22] Even a slight change in the method of synthesis and/or processing parameters along with precursor chemicals in the synthesis can result in variability in microstructure, crystal chemistry, and material properties.[14,16−22] For instance, Aziz et al. showed comparisons of the properties of $Dy^{3+}$-substituted cobalt ferrite between ultrasonication using ethanol and dry grinding, and the properties of magnetic materials changed.[30] Thus, as evident from the literature, the degree of inversion depends on heat treatment, synthesis method, concentration, and nature of substituted ions.[29,30]

The iron-rich cobalt ferrite, which can be represented by $Co_{1-x}Fe_{2+x}O_4$ ($x = 0.2$; referred to as Fe-CFO), materials are fascinating since they exhibit quite attractive features in addition to structural and electromagnetic properties that are desirable for numerous technologies. Fe-CFO exhibits pronounced magnetostrictive contraction; $\lambda = -590$ ppm has been reported for the (100)-oriented single crystal.[31−33] Iron-rich cobalt ferrite, $Co_{0.8}Fe_{2.2}O_4$, possesses higher magnetic anisotropy ($1.1 \times 10^6$ erg/cm$^3$)[34] accompanied by large anisotropic magnetostriction (∼166 to 200 ppm).[14,35] Moreover, it has been reported that the replacement of trivalent iron cation ($Fe^{3+}$) by rare-earth ions (such as $Dy^{3+}$, $Er^{3+}$, $Gd^{3+}$) in the spinel structure causes structural deformation, which induces strain in the lattice.[33,36] Furthermore, $Co_{0.8}Fe_{2.2}O_4$ is the most attractive composition due to its higher stress sensitivity. Also, dysprosium single crystal has shown a higher magnetostriction coefficient (7500 ppm). Thus, if dysprosium is considered for substitution for ferric ions in Fe-rich $Co_{0.8}Fe_{2.2}O_4$ composition, enhancement in magnetic properties is expected. Therefore, and also due to their ability to obtain desirable properties by simple means, the Fe-rich composition of Co-ferrite ($Co_{0.8}Fe_{2.2}O_4$) has been considered for technological applications by tuning their properties. For example, Shen et al. have reported excellent electromagnetic absorption properties of $Co_{0.8}Fe_{2.2}O_4$ integrated with graphene oxide.[17] Khodaei et al. reported that the (111)-oriented $Co_{0.8}Fe_{2.2}O_4$ thin films show higher coercivity in addition to enhanced saturation magnetization and squareness ratio.[21] Yang et al. reported that $Co_{0.8}Fe_{2.2}O_4$ synthesized using a sol−gel chemical method exhibits a higher saturation magnetization, up to 61.96 emu g$^{-1}$.[23] Baik et al. have reported that (111)-oriented $C_{0.8}Fe_{2.2}O_4$ single-layer films have a strong in-plane magnetic anisotropy as a result of orientation and stress-induced magnetic anisotropy.[20] Zi et al. reported that the $Co_{0.8}Fe_{2.2}O_4$ films, which were prepared by chemical solution deposition, can be used for recording and magneto-optical applications.[19] Similarly and specific to this particular topic, based on our extensive studies on intrinsic CFO, as reported previously elsewhere, it is observed that CFO has the highest strain sensitivity, ($d\lambda/dH$) ∼1.432 nm/A (for $H \leq 1000$ Oe).[14] From these considerations, it is appealing to further investigate Fe-rich CFO and explore new avenues for possible enhancement in properties and performance by means of suitable dopants/cations.

Considering the doping or substitution of metal ions into CFO, rare-earth metal (RM) ions play a vital role.[14,33] As documented widely in the literature, depending on the size and nature, the RM-ions introduce considerable lattice strain in CFO.[14,33] The lattice strain broadly improves magnetic properties and magnetostrictive properties, which are quite attractive for the design and development of magneto-mechanical sensors in addition to electromagnetic filters and antennas.[33] It was demonstrated that the Dy-substituted ferrite exhibits high strain sensitivity ($d\lambda$/dH), high resistance, and high magnetostriction values.[14] All of these interesting properties make Fe-rich cobalt ferrites favorable even for advanced electromagnetic and ME composite applications. However, while such efforts are critical, the fundamental aspects, especially the cation distribution and its influence on magnetic and dielectric properties, of rare-earth ion-substituted Fe-CFO are not well understood at this time. Therefore, the present work was focused on elucidating the effect of Dy substitution on the structural, magnetic, and dielectric properties of Fe-rich CFO nanomaterials. The Dy substitution in Fe-rich CFO has been considered a model system to deeply investigate the fundamental aspects of the structural chemistry, cation distribution/redistribution, crystallographic site preference of the dopant cation, and electromagnetic properties for the following reasons.

Among the lanthanide elements, theoretically, the magnetic moment is minimum (0 $\mu_B$) for $La^{3+}$ ion and maximum (10.5 $\mu_B$) for $Dy^{3+}$. The properties of lanthanide ions especially differ due to the *f*-electron density, which varies from element to element.[36,37] Thus, it is inspiring to explore the magnetic properties of dysprosium ($Dy^{3+}$) ion substituted at the $Fe^{3+}$ site in terms of the saturated magnetic moments or the *f*-electron density. Among all lanthanides, dysprosium ion ($Dy^{3+}$) has the maximum saturation magnetization value, which can be used to enhance magnetic parameters, such as saturation magnetization, remnant magnetization, etc.[36,38] Also, the relatively larger ionic size of $Dy^{3+}$ (0.912 Å) is expected to induce strain when substituted for a smaller $Fe^{3+}$ (0.64 Å) ion at the B-site.[14,36,38] Applications such as data storage require a squareness ratio close to 1 ($M_r/M_s \sim 1$). Stress sensitivity requires a higher rate of change of magnetization in a material as a result of the application of an external magnetic field ($dM/dH$).[14] Thus, it is expected that these requirements will be fulfilled by $Dy^{3+}$-substitution in CFO. The large magnetostrictive effect observed in dysprosium single crystals and the maximum linear strain of $\lambda = 7500$ ppm, at low temperature (5 K), are promising.[39] Furthermore, the substitution of larger $Dy^{3+}$ ions for smaller $Fe^{3+}$ at the octahedral site leads to increased scattering, which makes the ferrite material more resistive.[14,38] Such materials with enhanced electrical characteristics are quite useful in designing sensors for automotive applications.[40] However, the site occupation of cations in spinel lattice is sensitive to the method of preparation, processing parameters (rate of heating, rate of cooling, sintering time, and temperature), radii of cation being substituted, etc.[7,8,14] Therefore, while rare-earth ion substitution is highly promising, precise determination of the cation distribution and establishing a correlation between the structural and electromagnetic properties are critical for their utilization in practical device applications. This is the key objective of the present work performed on the synthesis and property evaluation of the Dy-substituted Fe-rich CFO (CFDO) nanomaterials.

We relied on the spectroscopic technique to accurately determine the cation distribution in CFDO nanomaterials. Mössbauer spectroscopy is one of the most sensitive techniques for determining the cation distribution of ferrites.[7,33] This analytical method has the highest resolution (1 in $10^{12}$) compared to all spectroscopic methods.[7,33,40,41] Therefore, an attempt is made to determine the cation distribution of all of the CFDO samples using Mössbauer spectroscopy, which is quite useful in studying ferrites. In connection with the Mössbauer studies, specifically on cobalt ferrites, reports existing in the literature shed light on the fundamental aspects of crystal chemistry and cation distribution. For instance, Meng et al. have reported the use of Mossbauer spectroscopy for the determination of the presence of double sextets corresponding to the A- and B-sites.[33] Moarris et al. studied the cobalt ferrites with Mössbauer spectroscopy to confirm the magnetic phase and also to reveal the magnetic ordering associated with the nanoparticles.[42] Gasemi et al. have concluded the substitution of Fe at the B-site based on the variation of the area of the B-site.[43] Gingasu reported the correlation of the hyperfine magnetic field at the Mössbauer nucleus with particle size and observed it to decrease with the decrease of particle volume.[44] Theoretical correlation between the cation distribution from Mössbauer spectroscopy was reported by Shan et al.[24] However, unfortunately, such an important theoretical study is not available for Fe-rich CFO with RM-ion, specifically $Dy^{3+}$, substitution. Further, to the best of our knowledge, either experimental or theoretical studies on the correlation of detailed cation distribution and magnetic properties for Fe-CFO are not available at this time. Therefore, for the first time, in the present work, an attempt is made to correlate the crystal structure, chemical distribution, and magnetic properties using combined Mössbauer spectroscopic studies with detailed Raman spectroscopic and magnetic measurements. The cation distribution along with Neel's two-sublattice model is used to calculate the saturation magnetization of all CFDO samples. Also, experimental values of saturation magnetization ($M_s$) in units of Bohr magneton per formula unit ($\mu_B$/f.u.) were obtained from magnetization versus magnetic field curves obtained using a superconducting quantum interface device (SQUID) magnetometer. Lastly, to determine the possible applications as a microwave absorption material, detailed dielectric measurements were made. We believe that the fundamental understanding of the crystal structure, cation distribution, magnetic properties, and structure−property correlation in the CFDO nanomaterials will contribute to the advancements in the field and apply to a large class of Fe-rich ferromagnetic nanomaterials for electromagnetic and sensor applications.

## ■ MATERIALS AND METHODS

**Synthesis.** Iron-rich cobalt ferrite ($Co_{0.8}Fe_{2.2-x}Dy_xO_4$) compounds with a variable concentration of $Dy^{3+}$ ($x = 0.000-0.100$, varying in small increments of 0.025) (referred to as CFDO) were prepared by a versatile autocombustion method, which is widely employed for nanoferrite synthesis.[14,16,22,36−38] Among the chemical methods available for the synthesis of nanoparticle ferrites, autocombustion is the most convenient and effective method, which involves lower reaction temperatures (80−100 °C) and rapid production with less time.[22,36,37] However, the quality and phase, especially at the nanoscale dimensions, depend on the synthesis conditions and precursor materials in addition to processing parameters.[14,16,22,36−38] Therefore, in this work, inexpensive metal nitrates of respective cations (Co, Fe, and Dy) are employed to produce CFDO inorganic compounds. For CFDO synthesis, analytical reagent (AR) grade cobalt nitrate hexahydrate $Co(NO_3)_2\cdot6H_2O$, iron nitrate $Fe(NO_3)_3\cdot9H_2O$, dysprosium nitrate pentahydrate $Dy(NO_3)_3\cdot5H_2O$, and anhydrous citric acid ($C_6H_8O_7$) precursors were taken as starting materials. Metal nitrates act as an oxidizer, and citric acid ($C_6H_8O_7$) acts as a fuel for burning the final gel formed in the autocombustion reaction. We adopted the previously established procedures and methods,[14,45] which are quite successful to synthesize rare-earth ion-substituted, Fe-rich CFO nanomaterials. For CFDO synthesis, the metal nitrates to fuel, i.e., oxidizer to fuel, ratio was maintained as 1:1 (stoichiometric). The ratio of oxidizers to fuel was calculated using the coefficients of oxidizing and reducing elements and valency.[46] The first step involved was accurately weighing cobalt nitrate, ferric nitrate, and dysprosium nitrate to prepare their solutions using deionized (DI) water as a solvent. These solutions were mixed using a magnetic stirrer with continuous stirring using a magnetic needle. After 15 min of continuous stirring without heating and uniform mixing of solutes, the citric acid solution was poured dropwise into the metal nitrate solution. The solution thus obtained was heated at temperatures of ∼120 to 130 °C, which changes the color of the solution from red to dark red.[12] After the water evaporated, the viscous complex gel was shifted to a hot plate at ∼300 °C, and the gel was completely burned with fire within a few seconds to yield the preferred powder ash. Finally, powders obtained were calcined within an alumina boat inside a tubular programmable furnace at 700 °C for 5 h by keeping the heating and cooling rate at 2 °C/min. The final sintered pellets are chemically stable compounds and nonhazardous.

**Characterization.** *Raman Spectroscopy.* Raman spectra were collected for CFDO compounds as a function of Dy concentration to understand the Dy substitution-induced effects. The measurements were made at room temperature using a Renishaw Invia Raman spectroscopy system LEICA DM 2500 M with a 532 nm green light Ar-ion LASER source. To obtain reliable information on the chemical bonding and structural information, the Raman scattering peaks were fitted using the standard procedures as widely reported in the literature.[41,47] Briefly, Raman spectra were fitted using the Lorentzian function

$$I(\omega) = I_0 + \frac{2A}{\pi}\left(\frac{W}{W + 4(\omega - \omega_0)^2}\right) \qquad (1)$$

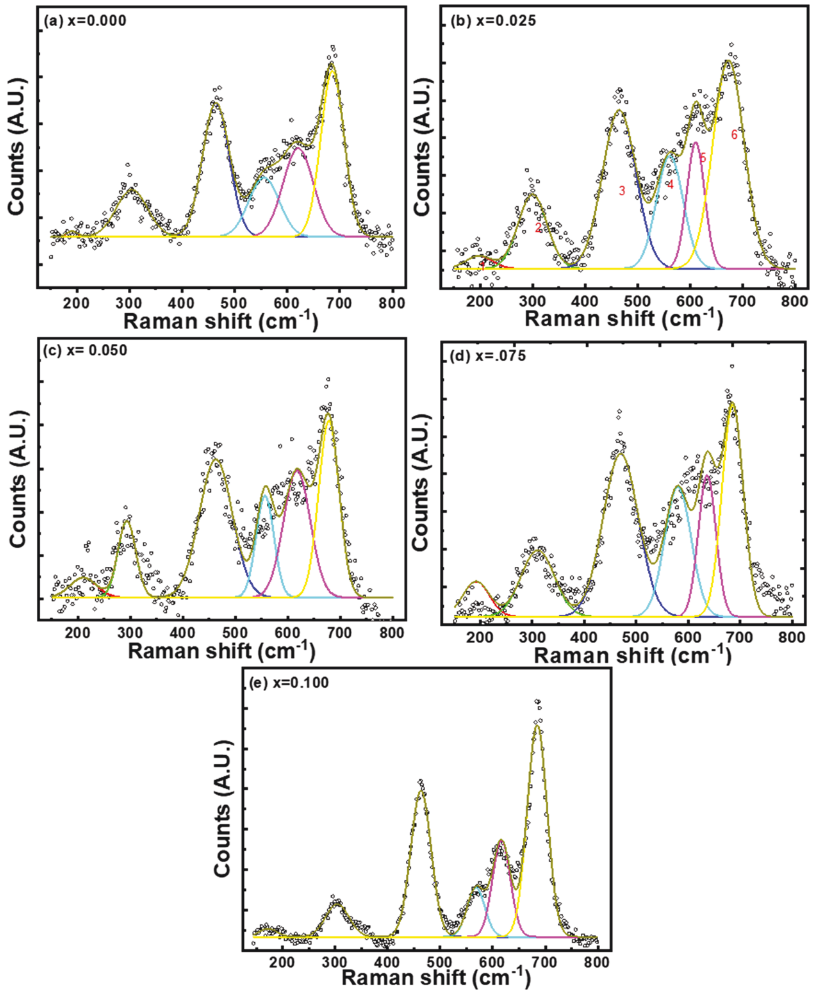

**Figure 2.** Raman spectra of $Co_{0.8}Fe_{2.2-x}Dy_xO_4$ nanomaterials. The data shown are for (a) $x = 0.000$, (b) $x = 0.025$, (c) $x = 0.050$, (d) $x = 0.075$, and (e) $x = 0.100$. The experimentally observed data and curve-fitted spectra are shown.

**Table 1. Raman Active Modes Observed for CFDO Compounds**[a]

| | | | observed Raman mode (cm$^{-1}$) | | | | |
|---|---|---|---|---|---|---|---|
| s. no. | Raman mode | reference mode (cm$^{-1}$) | $x = 0.000$ | $x = 0.025$ | $x = 0.050$ | $x = 0.075$ | $x = 0.100$ |
| 1 | $A_{1g}(1)$ | 695 | 684.1 | 684.5 | 677.7 | 683.2 | 685.2 |
| 2 | $A_{1g}(2)$ | 625 | 619.4 | 618.7 | 600.0 | 613.2 | 613.1 |
| 3 | $T_{1g}(1)$ | 575 | 552.2 | 534.5 | 532.7 | 601.5 | 609.5 |
| 4 | $T_{1g}(2)$ | 470 | 464.8 | 463.3 | 459.6 | 465.7 | 461.7 |
| 5 | $E_g$ | 312 | 344.7 | 301.3 | 295.5 | 305.7 | 307.7 |
| 6 | $T_{1g}(3)$ | 210 | 297.0 | | 217.8 | 176.1 | 176.3 |

[a] The experimental peak positions are compared with reference data.

where $\omega$ is the phonon frequency of the peak, "$\omega_0$" is the maximum phonon frequency of the peak, $W$ is full width at half-maxima (FWHM), "$A$" is the normalization constant, and "$I_0$" is the intensity of the background.

*Scanning Electron Microscopy (SEM).* Field-emission scanning electron microscopy (FESEM, Karl ZEISS JEOL) was used to characterize the microstructure and morphology of the CFDO compounds. The measurements were made on the CFDO compounds as a function of increasing Dy concentration. The energy-dispersive X-ray spectrometry (EDS) measurements were also made, using the same equipment, to understand and validate the chemical quality and composition of the samples. Platinum-coated CFDO samples were employed for EDS measurements while taking the Pt peak as a reference.

*Mössbauer Spectroscopy.* The room-temperature $^{57}$Fe Mössbauer measurements were made for all of the samples at zero magnetic field in a transmission geometry (Co$^{57}$ (Rh) radioactive source) using a standard PC-based Mössbauer spectrometer (WissEl - Wissenschaftliche Elektronik GmbH Germany). The velocity of the spectrometer was calibrated with the natural iron absorber at room temperature. Further, the recorded Mössbauer spectra were fitted using the NORMOS program.[41] Mössbauer spectra were recorded with a constant linear acceleration drive, along with a 512-channel analyzer using a $^{57}$Co radioactive source with 30 mCi activity. Calibration of the Mössbauer spectrometer was done using an enriched iron foil.

*Magnetic Measurements.* The magnetic hysteresis measurements were carried out using a SQUID magnetometer. The measurements were made at room temperature and 5 K.

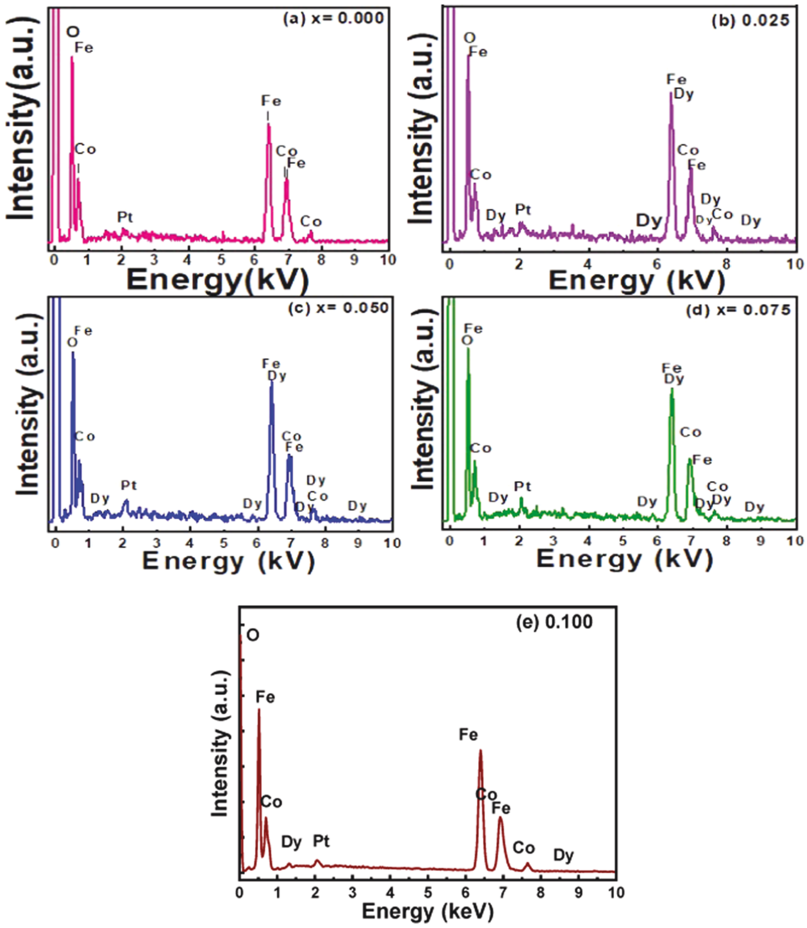

**Figure 3.** EDS data of $Co_{0.8}Fe_{2.2-x}Dy_xO_4$ compounds. The data shown are for (a) $x = 0.000$, (b) $x = 0.025$, (c) $x = 0.050$, (d) $x = 0.075$, and (e) $x = 0.100$. The characteristic X-ray peaks due to elements present in the samples are labeled in the figure.

*Dielectric Measurements.* A room-temperature dielectric constant versus frequency graph was obtained using a Hioki 3532-50 LCR HiTester meter in the frequency range from 50 Hz to 1 MHz.

## RESULTS AND DISCUSSION

**Chemical Quality and Chemical Bonding.** The chemical bonding and structural quality of the CFDO samples were probed using Raman spectroscopy, while the chemical composition was determined by the EDS analysis. The Raman spectra of CFDO samples are shown in Figure 2. The data shown are for CFDO materials with variable Dy concentration. The Raman active modes observed for all CFDO nanomaterials are summarized in Table 1. The experimental peak positions along with that of the ref 31 are shown (Table 1) for comparison. Group theory suggests 16 vibrational and rotational modes[48,49] for the spinel structure; these modes are $A_{1g}$(R), $F_g$ (R), $T_{1g}$, $3T_{2g}$ (R), $2A_{2u}$, $2F_u$, $4T_{1u}$ (IR), and $2T_u$. Among all modes, for Raman scattering, the only six modes active are $2A_{1g}$, $E_g$, and $3T_{2g}$.[48,50] The $A_{1g}(1)$ and $A_{1g}(2)$ modes were observed above 600 $cm^{-1}$ for all CFDO samples. These two modes are related to the symmetrical stretching and vibration of $Co^{2+}$ ion and $Fe^{3+}$ ion with $O^{2-}$ ion at the tetrahedral site of the spinel structure. On the other hand, the $E_g$ and $3T_{2g}$ modes observed below 600 $cm^{-1}$ for all CFDO samples are related to the symmetrical stretching of $Co^{2+}$ ion and $Fe^{3+}$ ion with $O^{2-}$ ion at the octahedral site of the spinel structure and are the results of the local lattice vibrations at the octahedral site.[48−50]

The experimental Raman scattering data can be used to discuss the structural quality and Dy-ion incorporation-induced effects in CFDO compounds. For all of the CFDO samples, comparing the relative peak intensities of the modes noted, the peak intensity is the highest for $A_{1g}(1)$. For bulk spinel ferrite, the highest intensity peak for octahedral site Raman active modes is reported at 470 $cm^{-1}$, while the tetrahedral site is at 695 $cm^{-1}$. For CFDO nanomaterials with variable Dy($x$) concentration up to 0.025, the peak noted is closer to 684 $cm^{-1}$, which is lower (nearly 1.6%). The peak shift toward the lower wavenumber may be due to lattice strain. With a further increase in $x$ values to 0.050, the peak with the highest intensity is further shifted to 677.7 $cm^{-1}$. This decrease (∼2.5%) is the maximum shift noted in this work for CFDO nanomaterials. This shift in tetrahedral site Raman modes can only be attributed to the lattice strain induced by $Dy^{3+}$-ion substitution. Peaks corresponding to the sample with $x = 0.050$ shifted to a lower value due to lower average particle size.[3] While the presence of desired Raman active modes indicates the formation of a spinel ferrite structure in Dy-substituted Fe-rich CFO nanomaterials, the peak shift is primarily due to the effect of Dy substitution. The relatively larger ionic radius of $Dy^{3+}$ substituting for the smaller ionic radius of $Fe^{3+}$ causes lattice distortion and, hence, lattice strain.

The general remarks about the effect of Dy substitution on the structural quality and chemical bonding in CFO nanomaterials can be further ascertained by comparison of the observed experimental Raman scattering data of CFDO with

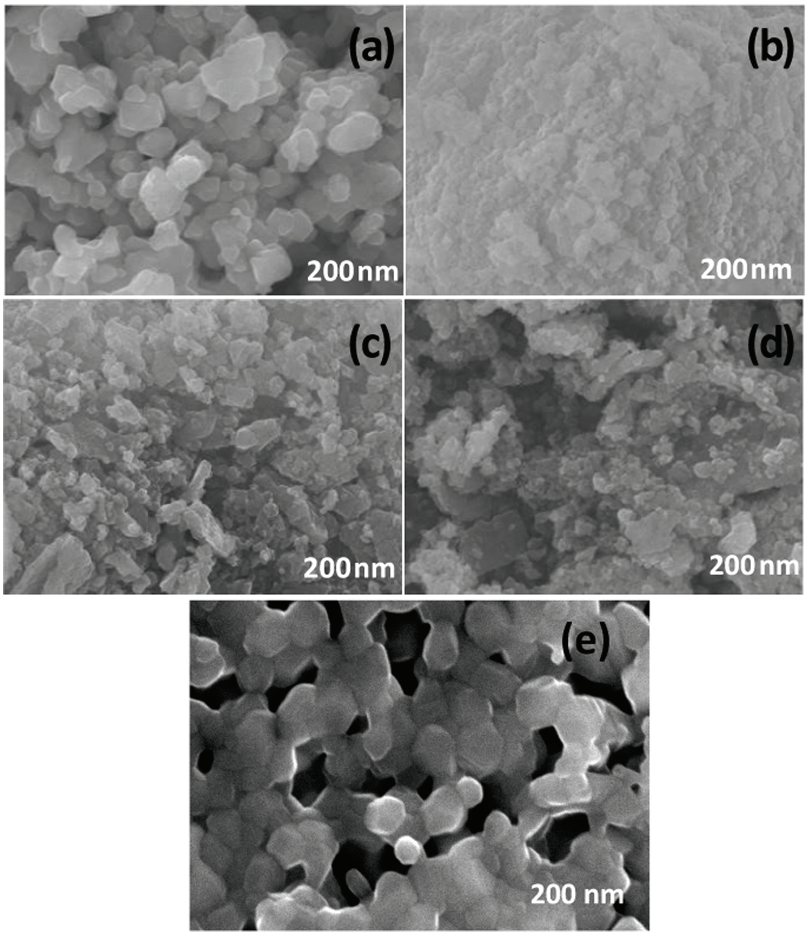

**Figure 4.** SEM images of $Co_{0.8}Fe_{2.2-x}Dy_xO_4$ compounds as a function of variable Dy concentration. The images shown are for (a) $x = 0.000$, (b) $x = 0.025$, (c) $x = 0.050$, (d) $x = 0.075$, and (e) $x = 0.100$.

other cation-substituted CFO as available in the literature. First of all, note that Raman spectroscopy is very sensitive to the changes in the structure and chemical bonding and provides accurate information on the chemical environment, bonding, particle size effects, etc.[1,51,52] Furthermore, it has been widely employed to evaluate the cation substitution effects, size effects, order−disorder, chemical inhomogeneities, and phase separation (if any) in ferrites.[2] Therefore, the peak shift noted in CFDO nanomaterials in the present work can be compared with the similar trend noted for CFO substituted with different cations. We believe that the red shift observed is due to lattice strain, which is a result of $Dy^{3+}$ ion substituting for $Fe^{3+}$ in the CFO lattice. This claim and its validity are further supported strongly by the Raman scattering peak shift reported independently for Er-, In-, and Mn-substituted CFO materials.[53−55] In these metal-ion-substituted ferrites, the lattice parameter expansion, which typically occurs due to dopant cation size compared to that of Fe, is accounted for the homogeneous strain in the crystal lattice leading to a Raman peak shift.[53−55] Therefore, in the present case, we believe that the Dy substitution-induced effects and strain in the lattice are dominant to account for the observed Raman peak shift. The chemical bonding and structure information probed by Raman scattering corroborates with the crystal structure and phase analysis of CFDO as reported previously.[14] Although such X-ray diffraction analysis and refinements were performed and confirmed, as reported previously, lattice constant enhancement was noted for $Dy^{3+}$ substitution. Among the lanthanide series of elements, $Dy^{3+}$ ions have f-electron density ($4f^9$) with large ionic radii (0.912 Å), and when they are substituted for smaller ionic radii $Fe^{3+}$(0.64 Å) ions, strain is induced in the compound.[56] Peaks corresponding to the sample with $x = 0.050$ shifted to a lower value due to lower average particle size. With the substitution of $Dy^{3+}$, the shift-increased intensity of spectra is observed.[57]

After the detailed chemical bonding and structural analysis of CFDO, the EDS measurements were used to understand their chemical composition and chemical homogeneity. The EDS spectra of CFDO nanomaterials are shown in Figure 3. The spectra show the X-ray peaks due to all anticipated (O, Fe, Co, Dy, along with Pt) elements. Thus, the EDS data reveal that the CFDO compounds are chemically homogeneous since the X-ray energy is characteristic of an individual element.[58] The spectra (Figure 3) indicate that the CFDO samples exhibit good chemical quality without any impurities incorporated during the synthesis.

**Microstructure and Morphology.** Figure 4 shows the SEM images highlighting the microstructure and morphology of CFDO nanomaterials as a function of Dy concentration. The CFDO samples with $x = 0.00$, i.e., without Dy substitution, show agglomerated particle size distribution. Typically, under the transition from bulk to nanoscale dimensions, ferrites drastically change the material's magnetic and structural properties, which are dependent on their particle

https://doi.org/10.1021/acs.inorgchem.2c03125
Inorg. Chem. 2022, 61, 19319−19332

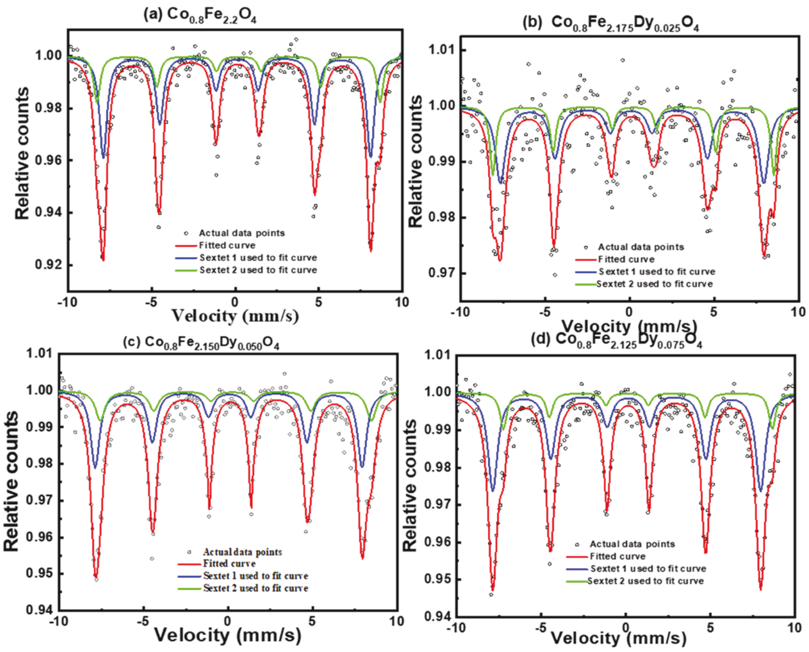

**Figure 5.** Mössbauer spectra of $Co_{0.8}Fe_{2.2-x}Dy_xO_4$ compounds. The spectra recorded for samples with variable Dy concentration. The data shown are for CFDO samples with (a) $x = 0.000$, (b) $x = 0.025$, (c) $x = 0.050$, and (d) $x = 0.075$ at 300 K.

**Table 2. Isomer Shift ($I_S$), Quadruple Splitting ($Q_S$), Hyperfine Field ($H_f$), and Half-Line Width ($\Gamma$) Obtained from Mossbauer Spectra for CFDO Samples**

| composition $x$ | (A)/(B) site | $I_S$(mm/s) | $Q_S$(mm/s) | $H_f$ (T) | $\Gamma$ (mm/s) |
|---|---|---|---|---|---|
| 0.000 | A | 0.103 ± 0.005 | −0.014 ± 0.010 | 49.553 ± 0.059 | 0.536 ± 0.022 |
| | B | 0.201 ± 0.013 | −0.017 ± 0.026 | 52.492 ± 0.104 | 0.459 ± 0.051 |
| 0.025 | A | 0.098 ± 0.020 | 0.059 ± 0.037 | 48.349 ± 0.203 | 0.714 ± 0.078 |
| | B | 0.232 ± 0.033 | −0.065 ± 0.057 | 51.591± 0.225 | 0.407 ± 0.148 |
| 0.050 | A | 0.052 ± 0.019 | −0.058 ± 0.029 | 48.996 ± 0.077 | 0.634 ± 0.036 |
| | B | 0.348 ± 0.056 | 0.205 ± 0.067 | 49.783 ± 0.139 | 0.685 ± 0.112 |
| 0.075 | A | 0.090 ± 0.021 | −0.097± 0.029 | 49.064 ± 0.010 | 0.679 ± 0.020 |
| | B | 0.385 ± 0.012 | 0.627 ± 0.020 | 49.265 ± 0.080 | 0.477 ± 0.078 |

size and particle size distribution.[1,59] In the present case, the particles of CFDO ($x = 0.00$) are highly agglomerated and nonuniform; such agglomeration is a result of their magnetic nature. The individual particle size varies from 25 to 300 nm. In all of the samples, a broad spread of the particle diameters occurs with an average particle diameter of about 100 nm. Initially, CFDO powder samples obtained by autocombustion synthesis were porous and agglomerated. This porosity of powders may be due to the sudden (less than 10 s) evaporation of an enormous amount of gases ($CO_2$, $H_2O$, etc.) during the autocombustion reaction.[35,60] The sample with $x = 0.050$ has smaller particle sizes and lesser interparticle distance as compared to other samples. This is what caused lower values of the Raman active modes as compared to the other samples (see Table 1). It has been reported that, on increasing the concentration of dysprosium in cobalt ferrite, the crystallite size decreases.[61] The average grain size calculated for all of the samples shows that there is a reduction in the average particle size with $Dy^{3+}$ substitution, but agglomeration is high for magnetic materials.

**Cation Distribution.** The room-temperature Mössbauer spectra of CFDO compounds are shown in Figure 5. On the $X$-axis, the velocity of the detector is given in mm/s, and the $Y$-axis indicates the intensity (in arbitrary units) of a number of $\gamma$ rays detected. The Mössbauer parameters, namely, the isomer shift ($I_S$), quadrupole splitting ($Q_S$), hyperfine field ($H_f$), and half-line width ($\Gamma$), are listed in Table 2. From Table 2, it is seen that the isomer-shift ($I_S$) values of $Dy^{3+}$-substituted Fe-rich CFO are observed to increase with the increase of $Dy^{3+}$ content at B-sites, and therefore isomer-shift values of B-sites are higher as compared to A-sites for all of the compositions. Furthermore, a decrease of the ferric ion ($Fe^{3+}$) concentration is observed with $x$ varying from 0.000 to 0.100. This may be ascribed to the removal of the outermost $4s^2$ electrons and one electron from $3d^6$ from the iron atom so that $Fe^{3+}$ is formed and, thus, the screening is reduced.[33] As a result, the electron density around ferric ($Fe^{3+}$) ions is observed to increase at B-sites due to $Dy^{3+}$ substitution (see Table 2). In addition, the distance between oxygen anion ($O^{2-}$) and metal cations ($Fe^{3+}$) at A-sites is shorter than that of the B-sites; thus, the isomer-shift value of the B-sites is higher than that of A-sites.[62] Further, it is well known that quadrupole splitting ($Q_S$) gives energy splitting due to the interaction between the nuclear energy levels and the surrounding gradient of the electric field. If the value of quadrupole splitting is positive, the shape of nuclear charge distribution is prolate, and if it is negative, the shape is oblate. In the present case, with the substitution of $Dy^{3+}$ at the $Fe^{3+}$ site in Fe-rich CFO, there may be a drastic change in the charge distribution, and as a result, the quadrupole splitting is changed. For instance, the magnitude

**Table 3. Cation Distribution Obtained from Mössbauer Spectral Analysis and the Saturation Magnetization Values**

| compositions $x$ | (A)/(B) site | area (mm$^2$) | cation distribution | saturation magnetization ($M_s$) from cation distribution ($\mu_B$/f.n.) | saturation magnetization ($M_s$) from the M−H curve at 5 K($\mu_B$/f.u.) |
|---|---|---|---|---|---|
| 0.000 | A | 0.749 | $[Fe_{1.00}]_A\ [Co_{0.80}Fe_{1.20}]_BO_4$ | 3.40 | 3.36 |
| | B | 0.250 | | | |
| 0.025 | A | 0.774 | $[Fe_{1.00}]_A\ [Co_{0.80}Fe_{1.175}Dy_{0.025}]_BO_4$ | 3.28 | 3.21 |
| | B | 0.225 | | | |
| 0.050 | A | 0.699 | $[Fe_{1.00}]_A\ [Co_{0.80}\ Fe_{1.150}\ Dy_{0.050}]_BO_4$ | 3.15 | 3.22 |
| | B | 0.316 | | | |
| 0.075 | A | 0.830 | $[Fe_{1.00}]_A\ [Co_{0.80}\ Fe_{1.125}\ Dy_{0.075}]_BO_4$ | 3.03 | 2.99 |
| | B | 0.153 | | | |

of $Q_S$ for the sample with $x$ = 0.025 ($CoFe_{2.175}Dy_{0.025}O_4$) becomes nearly four times more compared with the $Q_S$ value of the sample with $x$ = 0.000 ($CoFe_{2.2}O_4$) for both the B- and A-sites, and for the sample with $x$ = 0.075 ($CoFe_{2.125}Dy_{0.075}O_4$), the magnitude of $Q_S$ becomes nearly seven times and 37 times more compared with the $Q_S$ value of $CoFe_{2.2}O_4$ for the A- and B-sites, respectively. These results recommend that the $Dy^{3+}$ is substituted at the B-site (as expected), and as a result, we may expect that the charge distribution will be disturbed. The nuclear hyperfine field ($H_f$) for the sample with $x$ = 0.000 is 49.553 ± 0.059 T at the A-site and 52.492 ± 0.104 T at the B-site. From Table 2, it is apparent that the value of the hyperfine field first decreases for the sample with $x$ = 0.025 and then increases with further $Dy^{3+}$ substitution for the A-site. However, for the B-site, the value of $H_f$ is seen to continuously decrease as a result of a decreasing concentration of $Fe^{3+}$ at the B-site. The line width (Γ) gives a broadening of the peaks in Mössbauer.[63] For the sample with $x$ = 0.025, the line width is maximum for the A-site.

In the present study, two separate sextets were fitted to two sextets for different electron densities and nuclear fields of both the tetrahedral and octahedral site iron cations in accordance with[64]

$$\frac{(1+y)}{(1-x-y)} = \frac{n(\mathrm{Fe})_A}{n[\mathrm{Fe}]_B} \tag{2}$$

where $n(Fe)_A/n[Fe]_B$ is the ratio of the number of $_{26}Fe^{57}$ atoms at the A-site to $_{26}Fe^{57}$ atoms at the B-site. Further, $x$ is a composition of $Dy^{3+}$, and "$y$" is the inversion parameter. The ratio is calculated by taking the ratio of the area of a sextet of tetrahedral sites to the area of a sextet of octahedral sites. The cation distribution derived from Mössbauer spectral analyses is listed in Table 3. According to earlier reports, the cobalt ferrite system is mostly inverse spinel meaning that the $Co^{2+}$ ions mainly occupy the octahedral sites and $Fe^{3+}$ ions equally reside in tetrahedral and octahedral sites.[65] However, for the iron-rich CFDO system, we have observed that $Co^{2+}$ mostly occupied the B-site while $Dy^{3+}$ occupied the B-site. Although it has been previously reported that for the rare-earth-substituted $CoFe_2O_4$ phase, the ionic radii of $Dy^{3+}$ ions are larger compared to $Fe^{3+}$ ions and ions with larger ionic radii prefer to go to the B-site.[66] The perfect inverse spinel structure is obtained, and thus, the degree of inversion is complete for all CFDO samples. The cation distribution, determined from the Mössbauer studies, along with Neel's two-sublattice model, was used to calculate saturation magnetization. These saturation magnetization values match well with the saturation magnetization values obtained at low temperatures and high magnetic fields using the SQUID magnetometer. This is discussed in the next section.

The hyperfine field of $Fe^{3+}$ at the octahedral site is higher than that of $Fe^{3+}$ at the tetrahedral site for all of the samples. Similar results, which support our observations in this work, have been reported in the literature.[62] All of the recorded spectra show two overlapping six-line hyperfine spectra theoretically in a ratio of 3:2:1:1:2:3, corresponding to hyperfine splitting. But in this case, observed ratios are different for all CFDO samples. From these spectra, the ratio of a number of $_{26}Fe^{57}$ atoms at the tetrahedral site and octahedral site, i.e., $n(Fe)_A/n[Fe]_B$, of the area is calculated[67,68] (see Table 3). Here, $n(Fe)_A$ is the number of $_{26}Fe^{57}$ ions at the tetrahedral site, and $n[Fe]_B$ is the number of $_{26}Fe^{57}$ ions at octahedral sites. It is necessary to understand superexchange interaction to get a deeper understanding of the Mössbauer spectra.

Out of all possible superexchange interactions, only three AB, AA, and BB are considered. The AB interaction is the strongest, the AA and BB interactions between iron ions via oxygen ions are weaker, and all other possible interactions are generally considered to be the weakest.[62] Noticeable broadening is observed for the sample with $x$ = 0.025. Sixth-line overlap is not observed for all of the samples, which is indicated by the broadening of the absorption dip. Replacing $Dy^{3+}$ ions with $Fe^{3+}$ ions at a tetrahedral site reduces the superexchange interaction by a considerable amount.[62,67,69] A continuous decrease in the B-site hyperfine field from 52.49 ± 0.10 to 49.26 ± 0.00 T is observed with progressive $Dy^{3+}$ substitution. With the replacement of $Dy^{3+}$ for $Fe^{3+}$, the overall number of $Fe^{3+}$ cations in the CFDO compound decreases. Cation distribution reveals that $Dy^{3+}$ is substituted at the octahedral site in the Dy-incorporated Fe-rich cobalt ferrites. This is reflected by a decrease in the octahedral site hyperfine field. This may be due to the replacement of $Dy^{3+}$ for $Fe^{3+}$ ions at the octahedral site.[70] The substitution of $Dy^{3+}$ at the B-site is seen for the sample with $x$ = 0.075. According to earlier reports, Dy prefers octahedral void in the $CoFe_2O_4$ sample. But in the present case, due to iron-rich compositions, iron prefers octahedral sites compared to tetrahedral sites, and due to the overflow of Fe ions at the octahedral site, Dy ions prefer to go to octahedral sites.

From the Mössbauer spectrum, the presence of ferromagnetic $Fe^{3+}$ ions is identified at the A-site and B-site within the spinel structure. The distance between $O^{2-}$ and $Fe^{3+}$ in tetrahedral sites is ~0.67 Å, and in octahedral sites, ~0.72 Å. Less distance between $O^{2-}$ and $Fe^{3+}$ in the tetrahedral site corresponds to a greater overlap of the *s*-electron density of iron ion.[48,71] As the isomer-shift (IS) value of iron is inversely proportional to the *s*-electron density, the isomer-shift values of the octahedral sites are higher than those at tetrahedral sites.[72] Thus, the sextet that has higher values of both isomer shift (IS) and hyperfine field strength belongs to the $Fe^{3+}$ at octahedral sites, whereas the sextet that has lower values belongs to the $Fe^{3+}$ at the tetrahedral sites.[33,73] The isomer shift of $Fe^{3+}$at the tetrahedral site decreased with increasing Dy concentration at the B-site, indicating that the electron density decreased around Fe at the A-site. Since the quadrupole splitting for $Fe^{2+}$ ion ($>0.65$ $mms^{-1}$) is larger than that for $Fe^{3+}$($<0.65$ $mms^{-1}$), from the Mössbauer data, it is confirmed that $Fe^{2+}$ is absent in any of these CFDO compositions.[74]

**Magnetic Properties.** To confirm the cation distribution obtained from Mössbauer studies, M−H hysteresis loops as shown in Figure 6 are considered. The M−H data recorded by the SQUID magnetometer indicate that even after applying a maximum external magnetic field intensity of 1 Tesla, the magnetic hysteresis graphs are not saturated for any of the CFDO samples. This confirms the higher value of magnetocrystalline anisotropy of CFDO samples. The magnetic parameters such as saturation magnetization ($M_s$), remnant magnetization ($M_r$), coercivity ($H_c$), and squareness ratio ($M_r/M_s$) are obtained from M−H curves, which are shown in Table 4. The highest saturation magnetization ($M_s$) of 3.53 $\mu_B$/f.u. (Bohr magneton per formula unit) is obtained for the sample with $x = 0.100$. First, the squareness ratio (Mr/Ms) decreases with $Dy^{3+}$ content, then it reaches a minimum value for the sample with $x = 0.050$ and then increases for $x = 0.075$. This may be because anisotropic energy and thermal activation energy, $k_BT$, where $T$ is the temperature (K) and $k_B$ is the Boltzmann constant, become comparable for the CFDO sample with $x = 0.075$. Thus, magnetic moments are tilted away from the easy axis with the help of a small anisotropy energy barrier due to an external magnetic field and/or heat energy.[74,75] For the CFDO samples with $x = 0.075$, the magnetostatics energy might be reduced because many domains are arranged such that no poles exist at the surface and no lines of force go out of the material. The anomaly behavior of the sample with $x = 0.050$ is mainly due to smaller particle sizes compared to other samples.[3] The sample with $x = 0.100$ shows higher coercivity due to larger particle size distribution. When a large strain is generated due to the substitution of the $Dy^{3+}$ (0.912 Å) for $Fe^{3+}$(0.64 Å) at the B-site, the lattice strain is created, which can generate disorder in the crystal structure which may be responsible for the canting of magnetization and a decrease in magnetization values for the sample with $x = 0.025$ to $x = 0.075$.[30] Whereas the sample with $x = 0.100$ Dy concentration shows higher values of saturation magnetization, which may be due to the formation of an additional impurity phase $DyFeO_3$ with additional Dy−Dy interactions.[76]

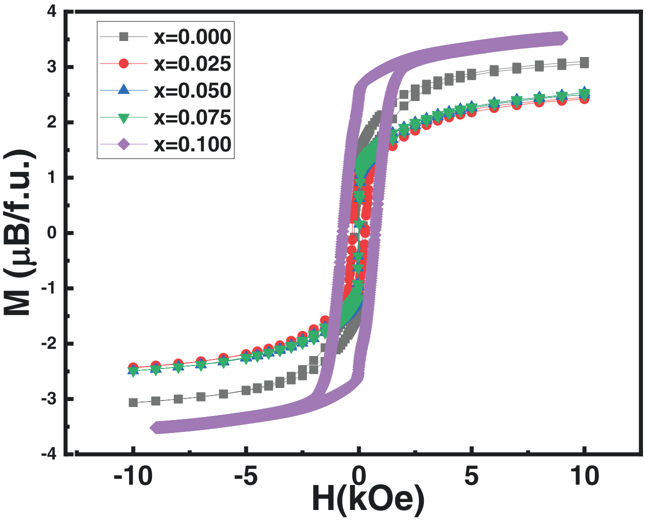

**Figure 6.** Magnetic (M−H) hysteresis loops of $Co_{0.8}Fe_{2.2-x}Dy_xO_4$ nanomaterials. The data shown are for CFDO samples with $x = 0.000$, $x = 0.025$, $x = 0.050$, $x = 0.075$, and $x = 0.100$. All of the data presented are obtained at 300 K.

Also, if the magnetic particle size approaches the nanometer scale, the magnetic properties of materials are strongly affected. Because of this, heat energy competes over the magnetic moment ordering.[77,78] The magnetization $\vec{M}$ values are converted from emu/gram to Bohr magneton per formula unit ($\mu_B$/f.u.) using the formula[65,79]

$$M(\text{in } \mu_B/\text{f. u.}) = \frac{[\text{molecular weight} \times M(\text{in emu/g})]}{5585} \tag{3}$$

where f.u. is a formula unit (one CFDO molecule), and $M$ is magnetization. The magnetic anisotropy constant $K$ plays a crucial role in explaining the magnetic properties of spinel ferrites.[75] The value of the anisotropic constant is calculated using the following formula[79]

$$K = \frac{M_s \times H_c}{0.96} \tag{4}$$

Anisotropy constant ($K$) data determined for CFDO compounds are tabulated in Table 4. As expected, high values of anisotropy constant ($K$) were obtained due to the occupation of octahedral sites by $Co^{2+}$ ions.[36,80] Ferrimagnetism of $Co_{0.8}Fe_{2.2}O_4$ is due to an antiferromagnetic intrasublattice exchange. The $Fe^{3+}$ ions at the tetrahedral and octahedral sites are antiferromagnetically coupled. When trivalent $Dy^{3+}$ is substituted for trivalent $Fe^{3+}$ ions at the octahedral sites, the antiferromagnetic coupling does not exactly cancel, as the number of ferric ions at tetrahedral and octahedral sites are unequal. This would alter the magnetization, as there is an extra contribution from the uncoupled $Fe^{3+}$ ions.[60] In the present study, Neel's two-sublattice model[78] fits for all of the CFDO samples, which is[36]

$$M_{\text{total}} = M_B(x) - M_A(x) \tag{5}$$

**Table 4. Magnetic Parameters Obtained from the M−H Hysteresis Loops at 300 K**

| composition $x$ | $M_s$($\mu_B$/f.u.) | $M_r$($\mu_B$/f.u.) | $H_c$ (Oe) | squareness ratio $M_r/M_s$ | anisotropy constant (K) (erg/cm$^3$) |
|---|---|---|---|---|---|
| 0.000 | 3.07 | 1.34 | 185.9 | 0.44 | $7.455 \times 10^6$ |
| 0.025 | 2.43 | 1.03 | 287.1 | 0.42 | $9.217 \times 10^6$ |
| 0.050 | 2.50 | 0.81 | 16.4 | 0.32 | $5.478 \times 10^6$ |
| 0.075 | 2.49 | 0.97 | 240.9 | 0.39 | $8.103 \times 10^6$ |
| 0.100 | 3.53 | 2.30 | 750 | 0.65 | $27.103 \times 10^6$ |

where $M_{total}$ is the resultant magnetic moment of the ferrimagnetic sample, and $M_B(x)$ and $M_A(x)$ are the octahedral and tetrahedral sublattice saturation magnetization, respectively. The values of Neel's magnetic moments ($M_{total}$) were obtained by taking the magnetic moment per ion of $Dy^{3+}$, $Fe^{3+}$, and $Co^{2+}$ as 10.5 $\mu_B$, 5 $\mu_B$, and 3 $\mu_B$, respectively. Initially, we tried to correlate the measured saturation magnetization values (at room temperature) with the magnetization values estimated from cation distribution derived from Mössbauer spectra, but they could not be matched. On the other hand, at low temperature ($T$) = 5 K and maximum applied external magnetic field intensity ($H$) = 50 kOe, the M−H curve undoubtedly shows a good correlation of the saturation magnetization data. Figure 7 shows the M−H curve of CFDO at 5 K. Table 4 shows the comparative data of saturation magnetic moments obtained from the SQUID magnetometer and cation distribution. Neel's two-sublattice model fits iron-rich ferrimagnetic CFDO samples. For all CFDO samples, the saturation magnetization value matches. Magnetization values for all of the compounds were lower as compared to the low-temperature magnetization. This may be attributed to lower values of the particle size distribution for all of the samples inducing superparamagnetic behavior.[81] The magnetization of the sample with $x = 0.100$ gradually increases and reaches a maximum value of 3.77 $\mu_B$/f.u. Also, the final sintering decreases coercivity and increases saturation magnetization with an increase in temperature.[82]

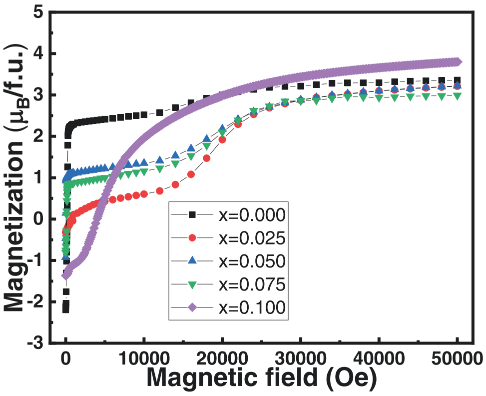

**Figure 7.** M−H curves obtained for $Co_{0.8}Fe_{2.2-x}Dy_xO_4$ nanomaterials. The data are measured at 5 K.

The squareness ratio ($M_r/M_s$) gives the direction of magnetization reorientation to the closest easy axis of magnetization direction after the magnetic field is switched off.[83] According to the Stoner−Wohlfarth theory, the squareness ratio value for ferrite nanoparticles is close to 0.5 and 0.83 for uniaxial and cubic anisotropy, respectively. Magnetic nanoparticles are known to exist in multimagnetic domain structures if the squareness ratio is greater than or equal to 0.5. For a sample with $x = 0.000$ to 0.075, the squareness ratio is less than 0.5, indicating that they are single-domain structures.[27] Whereas the sample with $x = 0.100$ has a higher value of squareness ratio, meaning it has multimagnetic domains. For the sample with $x = 0.050$, the value of coercivity is 16.4 Oe, which is the minimum, and the sample with $x = 0.100$ has a maximum, which is 750 Oe. The coercivity of a magnetic material is dependent on many factors, such as magnetic anisotropy, nonmagnetic ion substitution, density, grain size, macrostrain, and concentration of $Dy^{3+}$ ions.[28] An increase or decrease in the saturation magnetization values resulted from the superexchange interaction.[30] Magnetic anisotropy depends on multiple factors, such as the anisotropy of the cations, the symmetry of the interstitial sites, and cation distributions at A- and B-sites.

It is known that the saturation magnetization values depend on the cation distribution of the magnetic materials. Therefore, we have made a correlation of saturated magnetic values (refer to Table 3) obtained from the magnetic measurements and cation distribution derived from the Mössbauer spectra. $Dy^{3+}$ prefers to occupy the B-site, but due to its larger ionic size (compared with $Fe^{3+}$), it generates strain at the B-site. Thus, we expect that the resulting strain leads to an alteration of the cation distribution, and hence the saturation magnetization values are observed to fluctuate. We have analyzed the Mössbauer spectra and derived the cation distribution from which the saturation magnetization values are calculated. These magnetization values are found to be in good agreement (see Table 3) with the measured magnetization values.

**Dielectric Properties.** Figure 8 shows the dielectric constant versus frequency for all CFDO samples. With $Dy^{3+}$ substitution, an increase in the real part of the dielectric constant ($\varepsilon$) is observed. For all CFDO samples, the dielectric constant sharply decreases initially with higher values of frequency. The maximum value of the dielectric constant is obtained for the sample with $x = 0.075$. Comparing the value of the dielectric constant at 50 Hz, it is observed that with $Dy^{3+}$ substitution, a uniform increase in the dielectric constant is clearly visible. This is attributed to the higher resistance of the materials with $Dy^{3+}$ content and electron hopping.[38,72] According to the Maxwell−Wagner model, the dielectric constant of ferrite is contributed by larger conductive grains and smaller resistive grain boundaries.

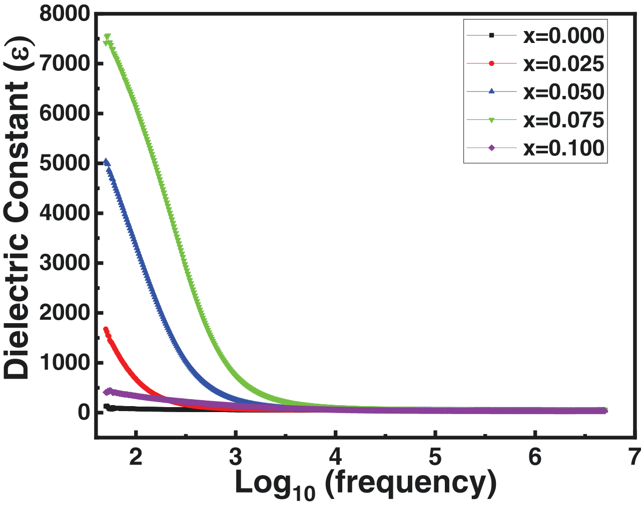

**Figure 8.** Dielectric constant of CFDO compounds. The data shown are frequency-dependent dielectric constants measured for CFDO compounds with variable Dy concentration.

Electron hopping at a low frequency between conductive grains causes polarization, which diminishes with high frequency because electrons cannot move with high frequency. This frequency is found to be 6.3 kHz for all CFDO samples. At high frequency (6 MHz), the dielectric constant becomes equal for all samples and it is 49 for all CFDO samples. The obtained values of the dielectric constant suggest that all

CFDO samples are suitable for microwave absorbers in high-frequency applications.

It is well known that the dielectric properties of the ferrites are due to the hopping of electrons between the grain boundaries. Maxwell−Wagner interfacial polarization[84−86] and Koop's phenomenological model[87] defined dielectric constant with frequency for spinel ferrites. According to these theories, it is expected that dielectric materials consist of two components as grains and grain boundaries. Large grains are of lower-resistance layers and, second, grain boundaries with high resistance. When an external electric field is applied to the dielectric materials, the electrons get trapped at the grain boundaries during hopping because of the high resistance of grain boundaries, which contributes to interfacial polarization. This is the reason for the resulting high dielectric constant (at lower frequencies) in magnetic materials. Further, Rabinkin and Novikova[88] proposed that the dielectric polarization in ferrites is also an equivalent mechanism to the conduction process. The electron hopping between ferric $Fe^{3+}$ and ferrous $Fe^{2+}$ ions produces the local displacement of electrons around the nucleus that generates polarization in ferrites. Therefore, at lower frequencies, the dielectric constant ($\varepsilon'$) has a higher value. With the increase in frequency, the polarization decreases, an exchange of electrons between $Fe^{2+}$ and $Fe^{3+}$ cannot respond to the ac electric field, and then the dielectric constant ($\varepsilon'$) decreases and becomes nearly constant. We have noticed that the dielectric constant of Fe-rich CFO increases with increasing $Dy^{3+}$ substitution. This may be ascribed to the ionic radius of $Dy^{3+}$ (0.912 Å) being larger than $Fe^{3+}$(0.64 Å) and $Co^{2+}$(0.74 Å). Therefore, for samples with $Dy^{3+}$ content ($x = 0.025$ to $x = 0.100$), dysprosium preferred to occupy the octahedral sites. Thus, with $Dy^{3+}$ substitution, the content of $Co^{2+}$ and $Fe^{3+}$ decreases at the octahedral sites. Further, the replacement of $Co^{2+}$ and $Fe^{3+}$ ions at octahedral sites by $Dy^{3+}$ ions increases the hopping rate between ferrous $Fe^{2+}$ and ferric $Fe^{3+}$ ions. Therefore, the polarization is observed to increase with increasing $Dy^{3+}$ content in ferrite samples, and as a consequence, there is a decrease in dielectric permittivity observed up to $x = 0.075$. However, for the sample with $x = 0.100$, a decrease in the dielectric constant is observed due to the presence of an additional $Fe_2O_3$ phase.

## ■ SUMMARY AND CONCLUSIONS

Dysprosium ($Dy^{3+}$)-substituted Fe-rich cobalt ferrite compounds were synthesized and characterized thoroughly by studying the structure, chemical bonding, microstructure and morphology, magnetism, and dielectric properties. Magnetization studies confirm the ferrimagnetic nature of all of the CFDO compounds. Mössbauer spectroscopic analyses allowed us to precisely determine the distribution of cations at A-site and B-site for all of the CFDO compounds with variable Dy concentration. The Mössbauer spectral analyses confirm the substitution of $Dy^{3+}$ at the B-site of the spinel structure. The Raman scattering analyses with a peak shift also validate the claim that $Dy^{3+}$ ions occupy the B-site leading to the strain of the CFDO compounds. To match the theoretical value of saturation magnetization, the low temperature (5 K) and high magnetic field (5 T) saturation magnetization values are required. These obtained values from the SQUID magnetometry experiment match well with the magnetization values obtained from cation distribution. Neel's two-sublattice model employed to estimate saturation magnetization ($M_s$) correlates well with the magnetic properties estimated with the aid of cation distribution obtained from Mössbauer data. Dielectric studies confirm the frequency above which the hopping of electrons stops to be 6.3 kHz. Dielectric results show that CFDO samples are useful for absorption in high-frequency applications. The present approach, which is based on combined Raman and Mössbauer spectroscopic analyses, successfully explains the chemical bonding and cation distribution and enhances our ability to derive a better understanding and correlation between the chemical, structural and magnetic properties for utilization of CFDO nanomaterials for sensor applications.

## ■ AUTHOR INFORMATION

### Corresponding Authors

**Yesh D. Kolekar** − *Department of Physics, Savitribai Phule Pune University, Pune 411007 Maharashtra, India;* orcid.org/0000-0002-9466-3184; Phone: +91-20-2569-2678; Email: ydkolekar@gmail.com; Fax: +91-20-2569-1684

**C. V. Ramana** − *Center for Advanced Materials Research (CMR) and Department of Mechanical Engineering, University of Texas at El Paso, El Paso, Texas 79968, United States;* orcid.org/0000-0002-5286-3065; Phone: +1-9157478690-2678; Email: rvchintalapalle@utep.edu; Fax: +1-9157475019

### Authors

**Shahaji P. Kharat** − *Department of Physics, Savitribai Phule Pune University, Pune 411007 Maharashtra, India; Department of Physics, Fergusson College (Autonomous), Pune 411004 Maharashtra, India*

**Swati K. Gaikwad** − *Department of Physics, Savitribai Phule Pune University, Pune 411007 Maharashtra, India; Department of Physics, Fergusson College (Autonomous), Pune 411004 Maharashtra, India*

**Rahul C. Kambale** − *Department of Physics, Savitribai Phule Pune University, Pune 411007 Maharashtra, India*

Complete contact information is available at: https://pubs.acs.org/10.1021/acs.inorgchem.2c03125

### Notes

The authors declare no competing financial interest.

## ■ ACKNOWLEDGMENTS

S.P.K. acknowledges the University Grants Commission (UGC) for providing a research fellowship under the Basic Scientific Research (BSR) scheme. S.P.K. and Y.D.K. acknowledge the Department of Science and Technology, India, for the research facilities developed through the grant (ref No. SR/FTP/PS-040/2010) to carry out the research work. CVR acknowledges, with pleasure, support from the National Science Foundation (NSF) with NSF-PREM grant #DMR-1827745.

## ■ REFERENCES

(1) Ansari, S. M.; Sinha, B. B.; Phase, D.; Sen, D.; Sastry, P. U.; Kolekar, Y. D.; Ramana, C. V. Particle Size, Morphology, and Chemical Composition Controlled $CoFe_2O_4$ Nanoparticles with Tunable Magnetic Properties via Oleic Acid Based Solvothermal Synthesis for Application in Electronic Devices. *ACS Appl. Nano Mater.* **2019**, *2*, 1828−1843.

(2) Bhame, S. D.; Joy, P. A. Effect of Sintering Conditions and Microstructure on the Magnetostrictive Properties of Cobalt Ferrite. *J. Am. Ceram. Soc.* **2008**, *91*, 1976−1980.

(3) Gómez, D. A.; Coello, J.; Maspoch, S. The influence of particle size on the intensity and reproducibility of Raman spectra of compacted samples. *Vib. Spectrosc.* **2019**, *100*, 48−56.

(4) Harada, M.; Kuwa, M.; Sato, R.; Teranishi, T.; Takahashi, M.; Maenosono, S. Cation Distribution in Monodispersed $MFe_2O_4$ (M = Mn, Fe, Co, Ni, and Zn) Nanoparticles Investigated by X-ray Absorption Fine Structure Spectroscopy: Implications for Magnetic Data Storage, Catalysts, Sensors, and Ferrofluids. *ACS Appl. Nano Mater.* **2020**, *3*, 8389−8402.

(5) Zhao, Q.; Yan, Z.; Chen, C.; Chen, J. Spinels: Controlled Preparation, Oxygen Reduction/Evolution Reaction Application, and Beyond. *Chem. Rev.* **2017**, *117*, 10121−10211.

(6) Hu, W.; Qin, N.; Wu, G.; Lin, Y.; Li, S.; Bao, D. Opportunity of spinel ferrite materials in nonvolatile memory device applications based on their resistive switching performances. *J. Am. Chem. Soc.* **2012**, *134*, 14658−14661.

(7) Sanchez-Lievanos, K. R.; Stair, J. L.; Knowles, K. E. Cation Distribution in Spinel Ferrite Nanocrystals: Characterization, Impact on their Physical Properties, and Opportunities for Synthetic Control. *Inorg. Chem.* **2021**, *60*, 4291−4305.

(8) Lyubutin, I. S.; Lin, C. R.; Starchikov, S. S.; Baskakov, A. O.; Gervits, N. E.; Funtov, K. O.; Tseng, Y. T.; Lee, W. J.; Shih, K. Y.; Lee, J. S. Structural, Magnetic, and Electronic Properties of Mixed Spinel $NiFe_{2-x}Cr_xO_4$ Nanoparticles Synthesized by Chemical Combustion. *Inorg. Chem.* **2017**, *56*, 12469−12475.

(9) Hähsler, M.; Landers, J.; Nowack, T.; Salamon, S.; Zimmermann, M.; Heissler, S.; Wende, H.; Behrens, S. Magnetic Properties and Mossbauer Spectroscopy of $Fe_3O_4/CoFe_2O_4$ Nanorods. *Inorg. Chem.* **2020**, *59*, 3677−3685.

(10) Shirsath, S. E.; Wang, D.; Zhang, J.; Morisako, A.; Li, S.; Liu, X. Single-Crystal-like Textured Growth of $CoFe_2O_4$ Thin Film on an Amorphous Substrate: A Self-Bilayer Approach. *ACS Appl. Electron. Mater.* **2020**, *2*, 3650−3657.

(11) Yadav, S.; Sharma, S.; Dutta, S.; Sharma, A.; Adholeya, A.; Sharma, R. K. Harnessing the Untapped Catalytic Potential of a $CoFe_2O_4$/Mn-BDC Hybrid MOF Composite for Obtaining a Multitude of 1,4-Disubstituted 1,2,3-Triazole Scaffolds. *Inorg. Chem.* **2020**, *59*, 8334−8344.

(12) Gumbi, S. W.; Mkwae, P. S.; Kortidis, I.; Kroon, R. E.; Swart, H. C.; Moyo, T.; Nkosi, S. S. Electronic and Simple Oscillatory Conduction in Ferrite Gas Sensors: Gas-Sensing Mechanisms, Long-Term Gas Monitoring, Heat Transfer, and Other Anomalies. *ACS Appl. Mater. Interfaces* **2020**, *12*, 43231−43249.

(13) Ratkovski, G. P.; do Nascimento, K. T. O.; Pedro, G. C.; Ratkovski, D. R.; Gorza, F. D. S.; da Silva, R. J.; Maciel, B. G.; Mojica-Sanchez, L. C.; de Melo, C. P. Spinel Cobalt Ferrite Nanoparticles for Sensing Phosphate Ions in Aqueous Media and Biological Samples. *Langmuir* **2020**, *36*, 2920−2929.

(14) Kharat, S. P.; Swadipta, R.; Kambale, R. C.; Kolekar, Y. D.; Ramana, C. V. Enhanced magnetostrictive properties of nanocrystalline $Dy^{3+}$ substituted Fe-rich $Co_{0.8}Fe_{2.2}O_4$ for sensor applications. *J. Appl. Phys.* **2017**, *122*, 164101.

(15) Hong, D.; Yamada, Y.; Sheehan, M.; Shikano, S.; Kuo, C.-H.; Tian, M.; Tsung, C.-K.; Fukuzumi, S. Mesoporous Nickel Ferrites with Spinel Structure Prepared by an Aerosol Spray Pyrolysis Method for Photocatalytic Hydrogen Evolution. *ACS Sustainable Chem. Eng.* **2014**, *2*, 2588−2594.

(16) Chang, H.; Kim, B. H.; Lim, S. G.; Baek, H.; Park, J.; Hyeon, T. Role of the Precursor Composition in the Synthesis of Metal Ferrite Nanoparticles. *Inorg. Chem.* **2021**, *60*, 4261−4268.

(17) Shen, W.; Ren, B.; Cai, K.; Song, Y.-f.; Wang, W. Synthesis of nonstoichiometric $Co_{0.8}Fe_{2.2}O_4$/reduced graphene oxide (rGO) nanocomposites and their excellent electromagnetic wave absorption property. *J. Alloys Compd.* **2019**, *774*, 997−1008.

(18) Zhang, H.; Gu, B.; Zhai, H.; Lu, M. Magnetic and magneto-optical properties of sputtered $Co_{0.8}Fe_{2.2}O_4$ films with perfect[111]-orientation. *Phys. Status Solidi A* **1994**, *143*, 399−404.

(19) Zi, Z. F.; Zhang, S. B.; Wang, B.; Zhu, X. B.; Yang, Z. R.; Dai, J. M.; Song, W. H.; Sun, Y. P. Morphology and magnetic properties of $Co_{0.8}Fe_{2.2}O_4$ films prepared by the chemical solution deposition. *J. Magn. Magn. Mater.* **2010**, *322*, 148−151.

(20) Khodaei, M.; Seyyed Ebrahimi, S. A.; Park, Y. J.; Choi, S. H.; Kim, C.; Son, J.; Baik, S. Thickness dependent magnetic properties of (111)-oriented $Co_{0.8}$ $Fe_{2.2}O_4$ thin film grown by pulsed laser deposition. *Thin Solid Films* **2014**, *571*, 62−68.

(21) Khodaei, M.; Seyyed Ebrahimi, S. A.; Park, Y. J.; Ok, J. M.; Kim, J. S.; Son, J.; Baik, S. Enhancement of in-plane magnetic anisotropy in (111)-oriented $Co_{0.8}Fe_{2.2}O_4$ thin film by deposition of PZT top layer. *Appl. Phys. A* **2014**, *117*, 1153−1160.

(22) Raghuvanshi, S.; Kane, S. N.; Lalla, N. P.; Reddy, V. R.Synthesis and Characterization of $Co_{0.8}Fe_{2.2}O_4$ Nano Ferrite, *Journal of Physics: Conference Series*, 2016; pp 1−5.

(23) Yang, L.; Xi, G.; Lou, T.; Wang, X.; Wang, J.; He, Y. Preparation and magnetic performance of $Co_{0.8}Fe_{2.2}O_4$ by a sol−gel method using cathode materials of spent Li-ion batteries. *Ceram. Int.* **2016**, *42*, 1897−1902.

(24) Shan, M.; Ding, S.; Hua, J.; Cui, W.; Wang, J.; Wang, J. Effect of annealing temperature on structure and magnetic properties of sol−gel synthesized $Co_{0.8}Fe_{2.2}O_4/SiO_2$ nanocomposites. *J. Sol-Gel Sci. Technol.* **2018**, *88*, 593−600.

(25) Niu, K.; Liang, L.; Peng, F.; Zhang, F.; Gu, Y.; Tian, H. Chelating-Template-Assisted in Situ Encapsulation of Zinc Ferrite Inside Silica Mesopores for Enhanced Gas-Sensing Characteristics. *ACS Appl. Mater. Interfaces* **2016**, *8*, 24682−24691.

(26) Calvo-de la Rosa, J.; Segarra Rubi, M. Influence of the Synthesis Route in Obtaining the Cubic or Tetragonal Copper Ferrite Phases. *Inorg. Chem.* **2020**, *59*, 8775−8788.

(27) Slimani, Y.; Almessiere, M. A.; Guner, S.; Aktas, B.; Shirsath, S. E.; Silibin, M. V.; Trukhanov, A. V.; Baykal, A. Impact of Sm($^{3+}$) and Er($^{3+}$) Cations on the Structural, Optical, and Magnetic Traits of Spinel Cobalt Ferrite Nanoparticles: Comparison Investigation. *ACS Omega* **2022**, *7*, 6292−6301.

(28) Atherton, D. L.; Beattie, J. R. A mean field Stoner-Wohlfarth hysteresis model. *IEEE Trans. Magn.* **1990**, *26*, 3059−3063.

(29) Naik, S. R.; Salker, A. V. Change in the magnetostructural properties of rare earth doped cobalt ferrites relative to the magnetic anisotropy. *J. Mater. Chem.* **2012**, *22*, 2740−2750.

(30) Aziz, C.; Azhdar, B. Synthesis of dysprosium doped cobalt ferrites nanoparticles by solgel auto-combustion method and influence of grinding techniques on structural, Morphological, and magnetic properties. *J. Magn. Magn. Mater.* **2022**, *542*, 168577.

(31) Chandramohan, P.; Srinivasan, M. P.; Velmurugan, S.; Narasimhan, S. V. Cation distribution and particle size effect on Raman spectrum of $CoFe_2O_4$. *J. Solid State Chem.* **2011**, *184*, 89−96.

(32) Prince, E. Neutron Diffraction Observation of Heat Treatment in Cobalt Ferrite. *Phys. Rev.* **1956**, *102*, 674−676.

(33) Meng, X.; Li, H.; Chen, J.; Mei, L.; Wang, K.; Li, X. Mössbauer study of cobalt ferrite nanocrystals substituted with rare-earth $Y^{3+}$ ions. *J. Magn. Magn. Mater.* **2009**, *321*, 1155−1158.

(34) Carvalho, M. H.; Lima, R. J. S.; Meneses, C. T.; Folly, W. S. D.; Sarmento, V. H. V.; Coelho, A. A.; Duque, J. G. S. Determination of the effective anisotropy constant of $CoFe_2O_4$ nanoparticles through the T-dependence of the coercive field. *J. Appl. Phys.* **2016**, *119*, 093909.

(35) Bhame, S. D.; Joy, P. A. Enhanced magnetostrictive properties of $CoFe_2O_4$ synthesized by an autocombustion method. *Sens. Actuators, A* **2007**, *137*, 256−261.

(36) Kumar, H.; Srivastava, R. C.; Pal Singh, J.; Negi, P.; Agrawal, H. M.; Das, D.; Hwa Chae, K. Structural and magnetic study of dysprosium substituted cobalt ferrite nanoparticles. *J. Magn. Magn. Mater.* **2016**, *401*, 16−21.

(37) Amiri, S.; Shokrollahi, H. Magnetic and structural properties of RE doped Co-ferrite (RE=Nd, Eu, and Gd) nano-particles

synthesized by co-precipitation. *J. Magn. Magn. Mater.* **2013**, *345*, 18−23.

(38) Almessiere, M. A.; Slimani, Y.; Gungunes, H.; Korkmaz, A. D.; Zubar, T.; Trukhanov, S.; Trukhanov, A.; Manikandan, A.; Alahmari, F.; Baykal, A. Influence of Dy($^{3+}$) Ions on the Microstructures and Magnetic, Electrical, and Microwave Properties of $[Ni_{0.4}Cu_{0.2}Zn_{0.4}]$-$(Fe_{2-x}Dy_x)O_4$ (0.00 </= x </= 0.04) Spinel Ferrites. *ACS Omega* **2021**, *6*, 10266−10280.

(39) Legvold, S.; Alstad, J.; Rhyne, J. Giant Magnetostriction in Dysprosium and Holmium Single Crystals. *Phys. Rev. Lett.* **1963**, *10*, 509−511.

(40) Rao, G. S. N.; Rao, B. P.; Hamdeh, H. H. Mossbauer Spectroscopic Study of High Magnetostrictive Cobalt Chromium Ferrites for Automobile Torque Sensors. *Procedia Mater. Sci.* **2014**, *6*, 1511−1515.

(41) Roy, S.; Ramana, C. V. Effect of sintering temperature on the chemical bonding, electronic structure and electrical transport properties of $\beta$-$Ga_{1.9}Fe_{0.1}O_3$ compounds. *J. Mater. Sci. Technol.* **2021**, *67*, 135−144.

(42) Morais, P. C.; Garg, V. K.; Oliveira, A. C.; Silva, L. P.; Azevedo, R. B.; Silva, A. M. L.; Lima, E. C. D. Synthesis and characterization of size-controlled cobalt-ferrite-based ionic ferrofluids. *J. Magn. Magn. Mater.* **2001**, *225*, 37−40.

(43) Ghasemi, A.; Paesano, A.; Cerqueira Machado, C. F.; Shirsath, S. E.; Liu, X.; Morisako, A. Mössbauer spectroscopy, magnetic characteristics, and reflection loss analysis of nickel-strontium substituted cobalt ferrite nanoparticles. *J. Appl. Phys.* **2014**, *115*, 17A522.

(44) Gingasu, D.; Mindru, I.; Ianculescu, A.-C.; Diamandescu, L.; Surdu, V.-A.; Marinescu, G.; Bartha, C.; Preda, S.; Popa, M.; Chifiriuc, M. C. Soft Chemistry Synthesis and Characterization of Co-$Fe_{1.8}RE_{0.2}O_4$ ($RE^{3+}$ = $Tb^{3+}$, $Er^{3+}$) Ferrite. *Magnetochemistry* **2022**, *8*, 12.

(45) Kakade, S. G.; Ma, Y.-R.; Devan, R. S.; Kolekar, Y. D.; Ramana, C. V. Dielectric, Complex Impedance, and Electrical Transport Properties of Erbium ($Er^{3+}$) Ion-Substituted Nanocrystalline, Cobalt-Rich Ferrite ($Co_{1.1}Fe_{1.9-x}Er_xO_4$). *J. Phys. Chem. C* **2016**, *120*, 5682−5693.

(46) Chavarriaga, E. A.; Lopera, A. A.; Franco, V.; Bergmann, C. P.; Alarcón, J. Gel combustion synthesis and magnetic properties of $CoFe_2O_4$, $ZnFe_2O_4$, and $MgFe_2O_4$ using 6-aminohexanoic acid as a new fuel. *J. Magn. Magn. Mater.* **2020**, *497*, 1−39.

(47) Xu, C. Y.; Zhang, P. X.; Yan, L. Blue shift of Raman peak from coated $TiO_2$ nanoparticles. *J. Raman Spectrosc.* **2001**, *32*, 862−865.

(48) Wang, Z.; Downs, R. T.; Pischedda, V.; Shetty, R.; Saxena, S. K.; Zha, C. S.; Zhao, Y. S.; Schiferl, D.; Waskowska, A. High-pressure x-ray diffraction and Raman spectroscopic studies of the tetragonal spinel $CoFe_2O_4$. *Phys. Rev. B: Condens. Matter Mater. Phys.* **2003**, *68*, 094101.

(49) Graves, P. R.; Johnston, C.; Campaniello, J. J. Raman scattering in spinel structure ferrites. *Mater. Res. Bull.* **1988**, *23*, 1651−1660.

(50) Modi, K. B.; Raval, P. Y.; Shah, S. J.; Kathad, C. R.; Dulera, S. V.; Popat, M. V.; Zankat, K. B.; Saija, K. G.; Pathak, T. K.; Vasoya, N. H.; Lakhani, V. K.; Chandra, U.; Jha, P. K. Raman and Mossbauer spectroscopy and X-ray diffractometry studies on quenched copper-ferri-aluminates. *Inorg. Chem.* **2015**, *54*, 1543−1555.

(51) Hussain, O. M.; Srinivasa Rao, K.; Madhuri, K. V.; Ramana, C. V.; Naidu, B. S.; Pai, S.; John, J.; Pinto, R. Growth and characteristics of reactive pulsed laser deposited molybdenum trioxide thin films. *Appl. Phys. A: Mater. Sci. Process.* **2003**, *207*, 135−138.

(52) Kalidindi, N. R.; Manciu, F. S.; Ramana, C. V. Crystal structure, phase, and electrical conductivity of nanocrystalline $W_{0.95}Ti_{0.05}O_3$ thin films. *ACS Appl. Mater. Interfaces* **2011**, *3*, 863−868.

(53) Ansari, S. M.; Ghosh, K. C.; Devan, R. S.; Sen, D.; Sastry, P. U.; Kolekar, Y. D.; Ramana, C. V. Eco-Friendly Synthesis, Crystal Chemistry, and Magnetic Properties of Manganese-Substituted $CoFe_2O_4$ Nanoparticles. *ACS Omega* **2020**, *5*, 19315−19330.

(54) Nongjai, R.; Khan, S.; Asokan, K.; Ahmed, H.; Khan, I. Magnetic and electrical properties of In doped cobalt ferrite nanoparticles. *J. Appl. Phys.* **2012**, *112*, 084321.

(55) Prathapani, S.; Vinitha, M.; Jayaraman, T. V.; Das, D. Effect of Er doping on the structural and magnetic properties of cobalt-ferrite. *J. Appl. Phys.* **2014**, *115*, 17A502.

(56) Ansari, M. M. N.; Khan, S.; Ahmad, N. Influence of $Dy^{3+}$ and Cu substitution on the structural, electrical and dielectric properties of $CoFe_2O_4$ nanoferrites. *J. Mater. Sci.: Mater. Electron.* **2019**, *30*, 17630−17642.

(57) Martens, J. W. D.; Peeters, W. L.; van Noort, H. M.; Erman, M. Optical, magneto-optical and mössbauer spectroscopy on $Co^{3+}$ substituted cobalt ferrite $Co_{2+}Fe_{2-x}Co_{3+x}O_4(0 \le x \le 2)$. *J. Phys. Chem. Solids* **1985**, *46*, 411−416.

(58) Ramana, C. V.; Ait-Salah, A.; Utsunomiya, S.; Becker, U.; Mauger, A.; Gendron, F.; Julien, C. M. Structural Characteristics of Lithium Nickel Phosphate Studied Using Analytical Electron Microscopy and Raman Spectroscopy. *Chem. Mater.* **2006**, *18*, 3788−3794.

(59) Vinitha Reddy Monaji, P. P. J. M. R.and Dibakar Das, Influence of cation distribution on the magnetic and dielectric properties of Zn doped CFO ceramicsInfluence of cation distribution on the magnetic and dielectric properties of Zn doped CFO ceramics, *AIP Conference Procedings*, 2016; pp 1−4.

(60) Kambale, R. C.; Song, K. M.; Koo, Y. S.; Hur, N. Low temperature synthesis of nanocrystalline $Dy^{3+}$ doped cobalt ferrite: Structural and magnetic properties. *J. Appl. Phys.* **2011**, *110*, 053910.

(61) Tsvetkov, M.; Milanova, M.; Ivanova, I.; Neov, D.; Cherkezova-Zheleva, Z.; Zaharieva, J.; Abrashev, M. Phase composition and crystal structure determination of cobalt ferrite, modified with Ce, Nd and Dy ions by X-ray and neutron diffraction. *J. Mol. Struct.* **2019**, *1179*, 233−241.

(62) Sawatzky, G. A.; Van Der Woude, F.; Morrish, A. H. Cation Distributions in Octahedral and Tetrahedral Sites of the Ferrimagnetic Spinel $CoFe_2O_4$. *J. Appl. Phys.* **1968**, *39*, 1204−1205.

(63) Ruby, S. L.; Hicks, J. M. Line Shape in Mössbauer Spectroscopy. *Rev. Sci. Instrum.* **1962**, *33*, 27−30.

(64) Thota, S.; Kashyap, S. C.; Sharma, S. K.; Reddy, V. R. Cation distribution in Ni-substituted $Mn_{0.5}Zn_{0.5}Fe_2O_4$ nanoparticles: A Raman, Mössbauer, X-ray diffraction and electron spectroscopy study. *Mater. Sci. Eng., B* **2016**, *206*, 69−78.

(65) Yadav, R. S.; Havlica, J.; Kuřitka, I.; Kozakova, Z.; Palou, M.; Bartoníčková, E.; Boháč, M.; Frajkorová, F.; Masilko, J.; Kalina, L.; Hajdúchová, M.; Enev, V.; Wasserbauer, J. Magnetic Properties of Dysprosium-Doped Cobalt Ferrite Nanoparticles Synthesized by Starch-Assisted Sol-Gel Auto-combustion Method. *J. Supercond. Nov. Magn.* **2015**, *28*, 2097−2107.

(66) Nikumbh, A. K.; Pawar, R. A.; Nighot, D. V.; Gugale, G. S.; Sangale, M. D.; Khanvilkar, M. B.; Nagawade, A. V. Structural, electrical, magnetic and dielectric properties of rare-earth substituted cobalt ferrites nanoparticles synthesized by the co-precipitation method. *J. Magn. Magn. Mater.* **2014**, *355*, 201−209.

(67) Keswani, B. C.; Patil, S. I.; Kolekar, Y. D.; Ramana, C. V. Improved magnetostrictive properties of cobalt ferrite ($CoFe_2O_4$) by Mn and Dy co-substitution for magneto-mechanical sensors. *J. Appl. Phys.* **2019**, *126*, 174503.

(68) Salazar-Tamayo, H.; García, K. E.; Barrero, C. A. New method to calculate Mössbauer recoilless f-factors in $NiFe_2O_4$. Magnetic, morphological and structural properties. *J. Magn. Magn. Mater.* **2019**, *471*, 242−249.

(69) Routray, K. L.; Sanyal, D.; Behera, D. Dielectric, magnetic, ferroelectric, and Mossbauer properties of bismuth substituted nanosized cobalt ferrites through glycine nitrate synthesis method. *J. Appl. Phys.* **2017**, *122*, 224104.

(70) Zipare, K. V.; Bandgar, S. S.; Shahane, G. S. Effect of Dy-substitution on structural and magnetic properties of Mn Zn ferrite nanoparticles. *J. Rare Earths* **2018**, *36*, 86−94.

(71) Wang, L.; Rai, B. K.; Mishra, S. R. Structural and magnetic study of $Al^{3+}$ doped $Ni_{0.75}Zn_{0.25}Fe_{2-x}Al_xO_4$ nanoferrites. *Mater. Res. Bull.* **2015**, *65*, 183−194.
(72) Almessiere, M. A.; Slimani, Y.; Shirsath, S. E.; Wudil, Y. S.; Baykal, A.; Ercan, I. Customized magnetic properties of $(Mn_{0.5}Zn_{0.5})$-$[Eu_xNd_xFe_{2-2x}]O_4$ nanospinel ferrites synthesized via ultrasonic irradiation approach. *Results Phys.* **2020**, *19*, 103350.
(73) Šepelák, V.; Bergmann, I.; Feldhoff, A.; Heitjans, P.; Krumeich, F.; Menzel, D.; Litterst, F. J.; Campbell, S. J.; Becker, K. D. Nanocrystalline Nickel Ferrite, $NiFe_2O_4$: Mechanosynthesis, Nonequilibrium Cation Distribution, Canted Spin Arrangement, and Magnetic Behavior. *J. Phys. Chem. C* **2007**, *111*, 5026−5033.
(74) Urcia-Romero, S.; Perales-Pérez, O.; Gutiérrez, G. Effect of Dy-doping on the structural and magnetic properties of Co−Zn ferrite nanocrystals for magnetocaloric applications. *J. Appl. Phys.* **2010**, *107*, 09A508.
(75) Rondinone, A. J.; Samia, A. C. S.; Zhang, Z. J. Superparamagnetic Relaxation and Magnetic Anisotropy Energy Distribution in $CoFe_2O_4$ Spinel Ferrite Nanocrystallites. *J. Phys. Chem. B* **1999**, *103*, 6876−6880.
(76) Yuan, X.; Sun, Y.; Xu, M. Effect of Gd substitution on the structure and magnetic properties of $YFeO_3$ ceramics. *J. Solid State Chem.* **2012**, *196*, 362−366.
(77) Andhare, D. D.; Patade, S. R.; Kounsalye, J. S.; Jadhav, K. M. Effect of Zn doping on structural, magnetic and optical properties of cobalt ferrite nanoparticles synthesized via. Co-precipitation method. *Phys. B* **2020**, *583*, 412051.
(78) Singhal, S.; Chandra, K. Cation distribution and magnetic properties in chromium-substituted nickel ferrites prepared using aerosol route. *J. Solid State Chem.* **2007**, *180*, 296−300.
(79) Jadhav, S. S.; Shirsath, S. E.; Patange, S. M.; Jadhav, K. M. Effect of Zn substitution on magnetic properties of nanocrystalline cobalt ferrite. *J. Appl. Phys.* **2010**, *108*, 093930.
(80) Franco, A.; e Silva, F. C. High temperature magnetic properties of cobalt ferrite nanoparticles. *Appl. Phys. Lett.* **2010**, *96*, 172505.
(81) Issa, B.; Obaidat, I. M.; Albiss, B. A.; Haik, Y. Magnetic nanoparticles: surface effects and properties related to biomedicine applications. *Int. J. Mol. Sci.* **2013**, *14*, 21266−21305.
(82) Chandra, G.; Srivastava, R. C.; Reddy, V. R.; Agrawal, H. M. Effect of sintering temperature on magnetization and Mössbauer parameters of cobalt ferrite nanoparticles. *J. Magn. Magn. Mater.* **2017**, *427*, 225−229.
(83) Gore, S. K.; Mane, R. S.; Naushad, M.; Jadhav, S. S.; Zate, M. K.; Alothman, Z. A.; Hui, B. K. Influence of $Bi^{(3+)}$-doping on the magnetic and Mossbauer properties of spinel cobalt ferrite. *Dalton Trans.* **2015**, *44*, 6384−6390.
(84) Aliuzzaman, M.; M M H; Jannatul Ferdous, M.; Manjura Hoque, S.; Abdul Hakim, M. Effect of Sintering Time on the Structural, Magnetic and Electrical Transport Properties of $Mg_{0.35}Cu_{0.20}Zn_{0.45}Fe_{1.94}O_4$ Ferrites. *World J. Condens. Matter Phys.* **2014**, *4*, 13−21.
(85) Maxwell, J. C.*Electricity and Magnetism*; Oxford University Press, 1973; Vol. *1*, pp 1−425.
(86) Frey, E.; Kroy, K. Brownian motion: a paradigm of soft matter and biological physics. *Ann. Phys.* **2005**, *517*, 20−50.
(87) Koops, C. G. On the Dispersion of Resistivity and Dielectric Constant of Some Semiconductors at Audiofrequencies. *Phys. Rev.* **1951**, *83*, 121−124.
(88) Ravinder, D. Dielectric behaviour of mixed lithium-zinc ferrites. *J. Mater. Sci. Lett.* **1992**, *11*, 1498−1500.